Source-Resolved Variability of Fine Particulate Matter and Human Exposure in an Urban Area

Pablo Garcia Rivera[1], Brian T. Dinkelacker[1], Ioannis Kioutsioukis[2],

Peter J. Adams[3,4], and Spyros N. Pandis[5,6]

[1]Department of Chemical Engineering, Carnegie Mellon University, Pittsburgh, PA, 15213

[2]Department of Physics, University of Patras, 26500, Patras, Greece

[3]Department of Civil and Environmental Engineering, Carnegie Mellon University, Pittsburgh, PA, 15213

[4]Department of Engineering and Public Policy, Carnegie Mellon University, Pittsburgh, PA, 15213

[5]Institute of Chemical Engineering Sciences (FORTH/ICE-HT), 26504, Patras, Greece

[6]Department of Chemical Engineering, University of Patras, 26500, Patras, Greece

Corresponding author: Spyros Pandis (spyros@chemeng.upatras.gr)

Abstract

Increasing the resolution of chemical transport model (CTM) predictions in urban areas is important to capture sharp spatial gradients in atmospheric pollutant concentrations and better inform air quality and emissions controls policies that protect public health. The chemical transport model PMCAMx was used to assess the impact of increasing model resolution on the ability to predict the source-resolved variability and population exposure to $PM_{2.5}$ at 36 x 36, 12 x 12, 4 x 4, and 1 x 1 km resolutions over the city of Pittsburgh during typical winter and summer periods (February and July 2017). At the coarse resolution, county-level differences can be observed, while increasing the resolution to 12 x 12 km resolves the urban-rural gradient. Increasing resolution to 4 x 4 km resolves large stationary sources such as power plants and the 1 x 1 km resolution reveals intra-urban variations and individual roadways within the simulation domain. Regional pollutants that exhibit low spatial variability such as $PM_{2.5}$ nitrate show modest changes when increasing

31   the resolution beyond 12 x 12 km. Predominantly local pollutants such as elemental carbon

32   and primary organic aerosol have gradients that can only be resolved at the 1 x 1 km scale.

33   Contributions from some local sources are enhanced by weighting the average contribution

34   from each source by the population in each grid cell. The average population weighted

35    $PM_{2.5}$ concentration does not change significantly with resolution, suggesting that

36   extremely high resolution $PM_{2.5}$ predictions may not be necessary for effective urban

37   epidemiological analysis.

1. Introduction

40   Particulate matter with aerodynamic diameter less than 2.5 µm ($PM_{2.5}$) contributes

41   to poor air quality throughout large parts of the United States. These particles directly affect

42   visibility (Seinfeld and Pandis, 2006) and have been associated with long and short-term

43   health effects such as premature death due to cardiovascular disease, increased chance of

44   heart attacks and strokes, and reduced lung development and function in children and

45   people with lung diseases such as asthma (Dockery and Pope, 1994).

46   At high resolutions, emissions from local sources such as commercial cooking, on-

47   road traffic, residential wood combustion, and industrial activities can have sharp gradients

48   that influence the geographical distribution of $PM_{2.5}$ concentrations. High-resolution

49   measurements of PM_1 have found gradients of up to ~2 µg m^{-3} between urban background

50   sites and those with high local emissions (Gu et al., 2018; Robinson et al., 2018).

51   A key limiting factor on the modeling of particulate matter at high resolutions is

52   the geographical distribution of emissions. Previous studies have found that coarse grid

53   emissions interpolated to higher resolutions lead to small to modest improvements in model

54   predictive ability for ozone (Arunachalam et al., 2006; Kumar and Russell, 1996),

55   secondary organic aerosol (Fountoukis et al., 2013; Stroud et al., 2011) and nitrate

56   (Zakoura and Pandis, 2019, 2018). Pan et al., (2017) used the default approach from the

57   U.S. Environmental Protection Agency (EPA) National Emissions Inventory (NEI) to

58   allocate county-based emissions to model grid cells at 4 x 4 and 1 x 1 km and found only

59   small changes to model performance for NO_x and O_3, while the 1 x 1 km case showed more

60   detailed features of emissions and concentrations in heavily polluted areas.

61   Improvements in the resolution of emission inventories have been focused on traffic
62   as this source exhibits significant variability at high resolutions. Recent approaches to
63   building high-resolution traffic inventories include origin-destination by vehicle class (Ma
64   et al., 2020), synthetic population mobility (Elessa Etuman and Coll, 2018) and fuel sales
65   combined with traffic counts (McDonald and McBride, 2014). Other sectors such as
66   biomass burning for residential heating and commercial cooking have been identified as
67   very uncertain in current inventories (Day et al., 2019). Recent versions of the NEI have
68   made progress addressing the total emissions and temporal distributions of biomass
69   burning and commercial cooking (Eyth and Vukovich, 2016), but there is still significant
70   uncertainty on their geographical location at a sub-county scale. Robinson et al. (2018)
71   found greatly elevated organic aerosol concentrations (10s of $\mu g\ m^{-3}$) in the vicinity of
72   numerous individual restaurants and commercial districts containing groups of restaurants
73   indicating that commercial cooking is a source of large gradients on the urban scale.

74   Population density and socio-economic indicators of that population, such as
75   income or access to healthcare, show large gradients in the urban scale. It is important to
76   assess the exposure of different sub-populations to air pollutants and the resulting health
77   effects, a concept known as Environmental Justice (Anand, 2002).

78   We use the Particulate Matter Comprehensive Air quality Model with Extensions
79   (PMCAMx) to study the impact of increasing model resolution on the model's ability to
80   predict the variability, sources and population exposure of $PM_{2.5}$ concentrations on the
81   urban scale in Pittsburgh. We compare predicted variability at 36 x 36, 12 x 12, 4 x 4 and
82   1 x 1 km resolutions over the city of Pittsburgh during one typical summer and one typical
83   winter month of 2017. Additional sensitivity simulations were performed to determine
84   contributions from selected sources to concentrations. The results of the simulations are
85   used to estimate exposure to $PM_{2.5}$ at all resolutions and from the selected sources. A
86   detailed evaluation of the PMCAMx predictions against measurements will be the topic of
87   a future publication. Overall the model performance was similar to those in previous model
88   applications in the Eastern US (Fountoukis et al., 2013).
89

2. PMCAMx Description

The Particulate Matter Comprehensive Air quality Model with Extensions (PMCAMx) (Karydis et al., 2010; Murphy and Pandis, 2009; Tsimpidi et al., 2010), uses the framework of the CAMx model (Environ, 2006) to describe horizontal and vertical advection and diffusion, emissions, wet and dry deposition, gas, aqueous and aerosol-phase chemistry. A 10-size section aerosol sectional approach is used to dynamically track the evolution of the aerosol mass distribution. The aerosol species modeled include sulfate, nitrate, ammonium, sodium, chloride, elemental carbon, water, primary and secondary organics, and other non-volatile aerosol components. The SAPRC (Statewide Air Pollution Research Center) photochemical mechanism (Carter, 1999) is used for the simulation of gas-phase chemistry. The version of SAPRC used here includes 237 reactions and 91 individual and surrogate species. For inorganic growth, a bulk equilibrium approach was used, assuming equilibrium between the bulk inorganic aerosol and gas phases (Pandis et al., 1993). Aqueous-phase chemistry is simulated using the Variable Size Resolution Model (VSRM) (Fahey and Pandis, 2001).The partitioning of the various semivolatile inorganic aerosol components and aerosol water is determined using the ISORROPIA-I aerosol thermodynamics model (Nenes et al., 1998). The primary and secondary organic aerosol components are described using the volatility basis set approach (Donahue et al., 2006). For primary organic aerosol (POA) ten volatility bins, with effective saturation concentrations ranging from 10^{-3} to $10^6\,\mu g\,m^{-3}$ at 298 K are used. The volatility distribution for POA from Tsimpidi et al. (2010) was used for all sources, while size distributions are specific to each emission sector. Anthropogenic (aSOA) and biogenic (bSOA) are modeled with 4 volatility bins (1, 10, 10^2, $10^3\,\mu g\,m^{-3}$) (Murphy and Pandis, 2009) using NO_x dependent yields (Lane et al., 2008). Both fine and coarse PM are simulated by PMCAMx, although the following analysis in this work is focused on fine PM. More detailed descriptions of PMCAMx can be found in Fountoukis et al. (2011) and Zakoura and Pandis (2018).

3. Model Application

PMCAMx was used to simulate air quality over the metropolitan area of Pittsburgh during February and July 2017. For the base-case simulation we used a one-way nested

121   structure with a 36 x 36 km master grid covering the continental United States, with nested

122   grids of 12 x 12 km, 4 x 4 km in South Western Pennsylvania and a 1 x 1 km grid covering

123   the city of Pittsburgh, most of Allegheny County and the upper Ohio River valley (Figure

124   1a). The 1 x 1 km grid covers a 72 x 72 km area (Figure 1b). Two days in each simulation

125   were used for model spin-up and discarded for all analyses. Simulations required

126   approximately 6 CPU days, 5 CPU hours, 10 CPU hours, and 12 CPU days to complete in

127   a single Intel Xeon CPU E5-4640 at 2.4 GHz for the 36 km, 12 km, 4 km, and 1 km

128   domains, respectively.

129   The surface concentrations at the boundaries of the 36 x 36 km grid are shown in

130   Table S1 in the Supplementary Information. These values were applied to all upper air

131   layers assuming a constant mixing ratio. Results from lower resolution simulations were

132   used as boundary conditions for the corresponding next higher resolution simulation.

133   Horizontal wind components, vertical diffusivity, temperature, pressure, water vapor,

134   clouds, and rainfall were generated using the Weather Research and Forecasting (WRF

135   v3.6.1) model over the whole modeling domain with horizontal resolution of 12 km. The

136   data was interpolated to higher resolutions when needed. The interpolation of

137   meteorological fields from 12 x 12 km to higher resolutions is a potential limitation of this

138   work and will be the focus of future improvements to the modeling methods. Initial and

139   boundary meteorological conditions for the WRF simulations were generated from the

140   ERA-Interim global climate re-analysis database, together with the terrestrial data sets for

141   terrain height, land-use, soil categories, etc. from the United States Geological Survey

142   (USGS) database. The WRF modeling system was prepared and configured in a similar

143   way as described by Gilliam and Pleim (2010). This configuration is recommended for air

144   quality simulations (Hogrefe et al., 2015; Rogers et al., 2013). 28 vertical layers were used

145   in the WRF simulations to produce 14 layers of meteorological input for the PMCAMx

146   simulations. Each of the 14 PMCAMx layers corresponds to a WRF layer.

147   Emissions were calculated using the EPA's Emission Modeling Platform (v6.3) for

148   the National Emissions Inventory for 2011 (NEI11) (Eyth and Vukovich, 2016) using the

149   default 2017 projected values. Base emissions were calculated first at a 12 km resolution

150   for the full modeling domain using the Sparse Matrix Operator Kernel Emissions

151   (SMOKE) model and our WRF meteorological data. The data sources used to produce 12

152 km resolution surrogates with Platform v6.3 were used to develop surrogates at 4 x 4 km

153 and 1 x 1 km resolution for all sectors except commercial cooking and on-road traffic for

154 which custom surrogates were developed. These custom surrogates also use projected

155 values for 2017. Bicubic interpolation was used to produce biogenic emissions at 4 x 4 km

156 and 1 x 1 km resolution, in areas in which sufficient data was unavailable. The emissions

157 by all sources together with the chemical composition are summarized in Tables 1 (for the

158 winter period) and 2 (for the summer period)..

159   In this work, we used normalized restaurant count to distribute the commercial

160 cooking emissions in space in the 1x1 km and 4x4 km resolution domains. Geographical

161 information was collected for all locations labeled as "restaurant" from the freely

162 accessible Google Places Application Programming Interface (API) for the western

163 Pennsylvania area, eastern Ohio and northern West Virginia. Using this new spatial

164 surrogate, $PM_{2.5}$ emissions from commercial cooking are enhanced primarily in the

165 Pittsburgh urban core with a maximum increase of 1200 kg d^{-1} km^{-2} (Figure 2a).

166   To accurately capture spatial patterns of on-road traffic, we use the output of a link-

167 level, origin-destination by vehicle class traffic model of Pittsburgh (Ma et al., 2020). This

168 traffic model simulates traffic counts and speed by hour-of-day using observations from

169 Pennsylvania Department of Transportation sites throughout Pittsburgh. As expected,

170 emissions in areas with major highways are high (Figure 2b).

171   The novel surrogates used for onroad traffic and cooking result in increases in

172 emissions in some areas and particularly in downtown Pittsburgh and decreases in others.

173 Total emissions inside the inner 1 x 1 km domain are the same using both the new and old

174 surrogates. For commercial cooking, emissions calculated using the new surrogates are

175 more concentrated in areas with high restaurant densities such as downtown Pittsburgh and

176 the Oakland neighborhood (Figures S1 and S2). For onroad traffic, the emissions become

177 higher at the locations of major highways and in the urban area of Pittsburgh when using

178 the new surrogates (Figures S3 and S4). Using the new spatial distribution of emissions

179 predicted average $PM_{2.5}$ increase by 1-2 µg m^{-3} at certain areas. A detailed evaluation of

180 these predictions will be the topic of another publication.

181

4. PM$_{2.5}$ concentrations and sources during winter

4.1 Effect of grid resolution

The results of the simulations with the four resolutions for the winter period are shown in Figures 3 and 4. For the area of interest, the simulations at 36 x 36 km resolves concentration fields at the county scale. The urban-rural gradient is resolved in the 12 x 12 km simulations. Increasing the resolution to 4 x 4 km, large stationary sources such as power plants and large industrial installations are resolved. Finally, the resolution increase to 1 x 1 km resolves the intra-urban variations in Pittsburgh and medium-sized industrial installations. Variable concentration limits are used in the species maps to remove background and highlight the effects of local sources (Figures 3 and 4).

In the winter period, the predicted maximum PM$_{2.5}$ concentration in the inner domain increases from 10.4 µg m^{-3} at 36x36 km, to 11.8 µg m^{-3} at 12x12, to 12.9 µg m^{-3} at 4x4, and finally to 16.4 µg m^{-3} at 1x1 km (Figure 3), a 58% increase. On the other end, the predicted minimum PM$_{2.5}$ concentration changes from 8.2 µg m^{-3} at 36 x 36 km to 7 µg m^{-3} at 12 x 12 and remains practically the same at even higher resolutions. This corresponds to the "background" concentration level for the area during the simulation period, so further resolution enhancements do not change this value. The standard deviation of the predicted concentration can be used as a measure of the concentration variability in the area. This standard deviation changes from 0.9 µg m^{-3} at 36x36, to 1.24 µg m^{-3} at 12x12, to 1.45 µg m^{-3} at 4x4 and to 1.35 µg m^{-3} at 1x1 km. These results indicate an increase of the PM$_{2.5}$ variability by 50% when one moves from the coarse to the finest resolution. However, most of this change in variability (38% out of the 50%) appears when one moves from 36x36 to 12x12 km.

Elemental carbon is a primary aerosol component with sources that are quite variable in space. In winter, the predicted maximum PM$_{2.5}$ EC increased by a factor of 2.9, from 0.6 µg m^{-3} at the 36 x 36 km resolution to 1.6 µg m^{-3} at 1 x 1 km (Figure 3). The predicted maximum EC is, as expected in the Pittsburgh downtown area. On the other hand, the predicted minimum of EC is reduced by only 0.1 µg m^{-3}, from 0.34 µg m^{-3} at 36x36 km to 0.24 µg m^{-3} at resolutions lower or equal than 4x4 km. The standard deviation of the predicted EC almost doubles from 0.1 µg m^{-3} at 36 x 36 km to 0.18 µg m^{-3} at 1 x 1 km. Approximately 50% of this increase in variability appears in the transition from the coarse

213 to the intermediate resolution of 12 x 12 km. The fine and the finest resolutions are needed

214 to resolve the other half of the predicted variability.

215 During this winter period a significant fraction (79%) of the OA in the Pittsburgh

216 area is primary and therefore the higher resolution results in increases of the predicted

217 maximum concentrations in space from 2.8 μg m^{-3} at the coarse resolution to 3.7 μg m^{-3} at

218 the intermediate to 4.8 μg m^{-3} at the finest resolution (Figure 3). This corresponds to an

219 increase by a factor of 1.7, more than the change for total PM$_{2.5}$, but much less than that

220 for EC. The predicted maximum is located in downtown Pittsburgh, with additional

221 hotspots in neighboring counties that are resolved at the fine and finest resolution. The

222 predicted minimum changes from 2.1 μg m^{-3} at 36x36 to 1.7 μg m^{-3} at 12x12 with small

223 reductions at higher resolutions. The variability (standard deviation) of the OA

224 concentration field of the predicted concentration increases by a factor of approximately

225 1.6 from 0.35 μg m^{-3} at 36 x 36, to 0.51 μg m^{-3} at 12 x 12 km. The increase is small at even

226 higher resolutions with the standard deviation of OA reaching 0.53 μg m^{-3} at 1 x 1 km (an

227 increase by a factor of 1.7).

228 Average predicted PM$_{2.5}$ sulfate in the inner domain changes little between the

229 coarsest resolution (average level 1.37 μg m^{-3}) and finest resolution (1.29 μg m^{-3}). The

230 minimum concentration decreased slightly with resolution from 1.33 to 1.2 μg m^{-3}, with

231 much of the decrease captured by increasing the resolution to 12 x 12 km. The maximum

232 sulfate concentration increased by a larger value but this change was not observed until

233 moving to the highest resolution where the maximum was 2.08 μg m^{-3}, compared to 1.4

234 μg m^{-3} at 36 x 36 km resolution. The standard deviation increased only marginally from

235 0.03 μg m^{-3} at 36 x 36 km to 0.06 μg m^{-3} at 1 x 1 km. The low variability in the predicted

236 ground sulfate levels during the winter is partially due to the low mixing heights during

237 this cold period with the emissions from the tall stacks of local power generation sources

238 often introduced above the boundary layer.

239 The predicted fine nitrate levels are relatively high ranging from 1.78 to 2.24 μg

240 m^{-3} in the coarse-resolution simulation. This is expected in this wintertime period due to

241 the partitioning of nitric acid and ammonium in the particulate phase. This predicted

242 concentration range increases to 1.5-2.24 μg m^{-3} in the finest scale simulation with higher

243 levels in the northeast of the domain. The standard deviation of the predicted concentration

244   does not show any significant trend changing from 0.19 µg m^{-3} at 36 x 36 to 0.15 µg m^{-3}

245   at 1 x 1 km.

246   For PM$_{2.5}$ ammonium, changes with increasing resolution are modest with the

247   predicted minimum being reduced from 1.07 µg m^{-3} at 36x36 to approximately 0.95 µg

248   m^{-3} at all other higher resolutions. The predicted maximum stays relatively constant

249   between 1.25 µg m^{-3} and 1.27 µg m^{-3} at all resolutions. As with nitrate, the standard

250   deviation does not show any significant trend changing from 0.08 µg m^{-3} at 36 x 36, to 0.09

251   µg m^{-3} at 12 x 12, to 0.07 µg m^{-3} at 4 x 4 and 1 x 1 km resolutions.

252

253   **4.2   Source Apportionment**

254   We performed zero-out simulations in the 1x1 km Pittsburgh grid to determine the

255   local contributions of eight source categories to the total PM$_{2.5}$. The local sources

256   quantified included: commercial cooking, industrial, biomass burning, on-road traffic,

257   power generation, and miscellaneous area sources. A summary of total local (within the

258   inner 1 x 1 km resolution domain) dry PM$_{2.5}$ emissions from each source category during

259   February 2017 is shown in Table 1. The species category labeled "other" for the power

260   generation sector is predominately composed of ash (including metals emitted from power

261   generation) and is simulated in PMCAMx as inert particle mass. Biomass burning

262   emissions here correspond only to residential wood combustion, as there were no

263   significant wildfiers in the 1 x 1 km resolution domain during the simulation periods. The

264   PM$_{2.5}$ emissions used in this study contain both the condensable and filterable fractions of

265   PM$_{2.5}$ (U.S. EPA, 2015). The miscellaneous area sources sector includes a large variety of

266   emission sources that are not classified in any of the sources in Table 1. These include

267   chemical manufacturing, solvent utilization for surface coatings, degreasing and dry

268   cleaning, storage and transport of petroleum products, waste disposal and incineration, and

269   cremation. The emissions from agricultural dust, river barges, off-road equipment, oil-gas

270   activities, and rail were grouped on the "others" source. All emissions (particulate and gas-

271   phase) from each source were set to zero, and the results of the zero-out simulation were

272   subtracted from those of the baseline simulation to estimate the corresponding source

273   contribution. The contribution of long-range transport from outside the inner domain was

274   also estimated by setting all local sources to zero.

275   Biomass burning is used during the winter for residential heating and recreation.
276   This source contributes a maximum of 3.31 µg m^{-3} in Cranberry, a northern suburb of
277   Pittsburgh located in the neighboring Butler county. In the downtown Pittsburgh area, the
278   contribution from biomass burning accounts for 7% of the PM$_{2.5}$. This source shows the
279   highest variability with a standard deviation of 0.5 µg m^{-3}.

280   The maximum contribution of 8.05 µg m^{-3} from industry is predicted near a cluster
281   of industrial facilities in the town of Beaver, 37 km northwest of Pittsburgh. The maximum
282   PM$_{2.5}$ concentration of the modeling domain is located here. In this location long-range
283   transport contributes 37% of the PM$_{2.5}$ followed by industrial sources with 49% and
284   biomass burning with 7%. On average, the contribution from industrial sources is low with
285   3.7%. In downtown Pittsburgh, the contribution is lower still with 2%.

286   On-road traffic emissions are most important in major highway intersections and
287   river crossings surrounding downtown Pittsburgh with a maximum contribution of 3.9 µg
288   m^{-3} accounting for 24% of the PM$_{2.5}$ in this area. On average, on-road traffic contributes
289   2.5% of the PM$_{2.5}$ mass. The contribution from on-road traffic shows higher variability
290   (standard deviation: 0.36 µg m^{-3}) since this sector contributes significantly to areas adjacent
291   to the network of highways that radiates from the Pittsburgh downtown.

292   On average, commercial cooking emissions contribute 0.7% of the PM$_{2.5}$ in the
293   modeling domain with a maximum contribution of 2.44 µg m^{-3} in downtown Pittsburgh,
294   with smaller contributions in the surrounding urban area. Cooking is predicted to account
295   for 16% of the PM$_{2.5}$ mass in downtown Pittsburgh. The contribution from commercial
296   cooking is localized around downtown Pittsburgh and therefore shows little variability
297   throughout the domain with a standard deviation of 0.1 µg m^{-3}.

298   The miscellaneous area source sector contributes 6% of the PM$_{2.5}$ on average. Since
299   this sector encompasses a variety of sources and activities, its contribution shows
300   significant variability with a standard deviation of 0.34 µg m^{-3}.The maximum contribution
301   is located in the Pittsburgh urban core with 1.64 µg m^{-3}, accounting for 11% of the PM$_{2.5}$.

302   The power generation sector contributes a maximum of 0.63 µg m^{-3} in the plume
303   of the Bruce Mansfield power plant northwest of Pittsburgh (this plant is no longer
304   operating as of 2019). The contribution of this sector shows the smallest variability at 0.09
305   µg m^{-3}. The contribution to ground PM$_{2.5}$ from power generation in the winter is relatively

306 low. This is largely due to the height of the emissions stacks associated with this sector. A
307 significant fraction of the emissions from power generation is trapped above the shallow
308 mixing height in the winte and much of the $PM_{2.5}$ mass is predicted to remain in the upper
309 air layers. The predicted relative high upper air $PM_{2.5}$ concentration from power generation
310 are shown in Figure S5.

311   Long-range transport from outside the inner modeling domain is the major source
312 of $PM_{2.5}$ during this period contributing an average of 74%. This contribution varies from
313 7.1 $\mu g\ m^{-3}$ in the southeast corner of the domain decreasing in the direction of the Pittsburgh
314 urban core where the contribution is reduced to 5.9 $\mu g\ m^{-3}$. In areas where there are
315 significant local emissions such as the Pittsburgh downtown, the contribution from long-
316 range transport decreases to 38%.

317   Contributions for all remaining sources are largest in the Pittsburgh downtown with
318 0.74 $\mu g\ m^{-3}$, accounting for 5% of the $PM_{2.5}$. This sector also significantly contributes on
319 the Ohio and Monongahela river valleys, where there is important rail and river traffic. On
320 average, these sources contribute 3% of the $PM_{2.5}$ and show a moderate variability with a
321 standard deviation of 0.1 $\mu g\ m^{-3}$.

322   For all local sources, the minimum contribution is close to zero (less than 0.1 μg
323 m^{-3}) and is located at the southwestern corner of the domain, near the Ohio – West Virginia
324 border.

325

326 **5. $PM_{2.5}$ concentrations and sources during summer**

327 **5.1 Effect of grid resolution**

328   The predicted $PM_{2.5}$ concentrations in the simulated summer period are lower than
329 during the winter period and more uniform, however, the qualitative behavior of the model
330 at the different scales remains the same (Figure 6). Variable concentration limits are again
331 used in these maps to remove background and highlight the effects of local sources. The
332 standard deviation of the $PM_{2.5}$ increases from 0.28 $\mu g\ m^{-3}$ at 36 x 36, to 0.57 $\mu g\ m^{-3}$ at 12
333 x 12, to 0.72 $\mu g\ m^{-3}$ at 4 x 4 and to 0.82 $\mu g\ m^{-3}$ at 1 x 1 km. At the finest scale, the predicted
334 variability in the summer is 61% of that in the winter. Similar to the winter period, the
335 predicted maximum $PM_{2.5}$ concentration changes significantly with increasing resolution.
336 The predicted maximum $PM_{2.5}$ increases from 6.4 $\mu g\ m^{-3}$ at the coarse to 15.3 $\mu g\ m^{-3}$ at the

337   fine resolution. The finest scale better resolves the concentration field in the cluster of
338   industrial installations 37 km northwest of Pittsburgh. The minimum $PM_{2.5}$ drops from 6.5
339   µg m^{-3} at 36 x 36 to 5.3 µg m^{-3} at 12 x 12, and then to 4.7 µg m^{-3} at 1 x 1 km. As in the
340   winter period, the moderate resolution appears to capture the majority of the concentration
341   change from increasing resolution (67%).

342   The average EC is lower during the summer with 0.28 µg m^{-3} versus 0.43 µg m^{-3}
343   in the winter. The standard deviation of the predicted average EC increases from 0.06 µg
344   m^{-3} at 36 x 36, to 0.09 µg m^{-3} at 12 x 12, to 0.11 µg m^{-3} at 4 x 4 km, and to 0.13 µg m^{-3} at
345   1 x 1 km. The peak average EC is located in downtown Pittsburgh and increases by a factor
346   of 3.6 (from 0.35 to 1.27 µg m^{-3}) moving from the coarse to the finest resolution. It is
347   noteworthy that the peak is 38% less than that of the winter when the coarse resolution is
348   used, but only 21% when the finest resolution is used. The concentration range (difference
349   between the maximum and the minimum) increases from 0.13 µg m^{-3} to 1.12 µg m^{-3}
350   moving from the coarse to the finest resolution. This increase by a factor of 8.6 shows the
351   importance of the local variations of a primary species like EC in an urban area in both
352   summer and winter.

353   The OA concentration field is quite uniform at the coarse-scale varying by only
354   0.17 µg m^{-3} (from 1.72 to 1.89 µg m^{-3}) with a standard deviation of 0.07 µg m^{-3} (Figure 6).
355   Variablility increases significantly when one moves to the finest scale, with the range
356   increasing to 2.24 µg m^{-3} (from 1.55 to 3.79 µg m^{-3}) and the standard deviation of the OA
357   field increases to 0.2 µg m^{-3}. The use of the finest scale appears to be needed for the
358   resolution of the OA high concentration areas in the summer more than in the winter.

359   The $PM_{2.5}$ sulfate levels during the summer period are on average 12% higher
360   during the summertime period. At the coarse and intermediate scales, the predicted average
361   concentration fields have relatively little structure (Figure 7). The corresponding
362   concentration ranges are relatively narrow (0.05 µg m^{-3} at 36 x 36 km and 0.42 µg m^{-3} at
363   12x12 km). However, a different picture emerges at the fine and especially the finest scales.
364   The plumes from the major power plants can be clearly seen at these higher resolutions.
365   The maximum increased by 0.5 µg m^{-3} from the coarse scale to the finest scale while the
366   minimum is reduced from 1.78 µg m^{-3} at 36 x 36 to 1.05 µg m^{-3} at 12 x 12, to 0.95 µg m^{-3}
367   at 4 x 4 and 1 x 1 km. The standard deviation of the predicted sulfate concentration field

368 at the coarse resolution is low and similar to that in winter, 0.02 µg m^{-3}. However, the
369 variability at the finest scale in the summer (0.13 µg m^{-3} at 1x1 km) is twice the predicted
370 variability in the winter.

371 The predicted summertime nitrate concentrations are quite low in the area (average
372 0.5 µg m^{-3} in the coarse and 0.46 µg m^{-3} in the finest resolution). The predicted minimum
373 decreases from 0.42 µg m^{-3} at 36 x 36 to 0.39 µg m^{-3} at 12 x 12, to 0.34 µg m^{-3} at 4 x 4, and
374 to 0.3 µg m^{-3} at 1 x 1 km. The predicted maximum concentration increases from 0.56 µg
375 m^{-3} at the coarse scale to 0.71 µg m^{-3} at the intermediate scale and stays relatively constant
376 at higher resolutions. The concentration field is quite uniform with a standard deviation
377 ranging from 0.06 to 0.09 µg m^{-3} for all scales. However, due to the reduction in the
378 predicted minimum the concentration range increases from 0.14 µg m^{-3} at the coarse
379 resolution to 0.37 µg m^{-3} at the finest resolution.

380 The PM$_{2.5}$ ammonium concentration field is quite uniform at all resolutions (Figure
381 7). The concentration range increases from 0.04 to 0.22 µg m^{-3} moving from the coarse to
382 the finest resolution and the standard deviation increases from 0.02 to 0.04 µg m^{-3}.

383

384 **5.2 Source Apportionment**

385 The local emissions for each source category during July 2017 are shown in Table
386 2. During summer, residential biomass burning is minimal. This source contributes a
387 maximum of 0.04 µg m^{-3} and an average of 0.007 µg m^{-3},accounting for 0.6% of the
388 average total PM$_{2.5}$.

389 Power generation sources have the highest average contribution to total PM$_{2.5}$ of
390 all the local sources of 10%. Industrial sources account for 6% of the average PM$_{2.5}$ but are
391 the most important contributor in the point of the modeling domain with the maximum
392 predicted PM$_{2.5}$ conentration. At this location in Beaver County, industrial sources account
393 for 58% of total PM$_{2.5}$

394 As in the winter period, on-road traffic emissions have the largest contribution to
395 the PM$_{2.5}$ in the downtown Pittsburgh area where four large highways intersect. In this
396 location on-road traffic contributes 26% of the PM$_{2.5}$. On average, local on-road traffic
397 contributes around 3% of the PM$_{2.5}$ mass. During the summer period, the variability of the

398   on-road traffic contribution is slightly lower with 0.33 µg m^{-3} compared with 0.36 µg m^{-3}

399   during winter.

400   Commercial cooking emissions contribute a maximum of 2.08 µg m^{-3} to the

401   average total PM$_{2.5}$ in downtown Pittsburgh. This source accounts for 17% of the PM$_{2.5}$ in

402   the city but only 1% for the entire modeling domain. The large predicted contribution from

403   cooking PM$_{2.5}$ is consistent with the mobile AMS measurements performed by Ye et al.

404   (2018), that indicated that cooking organic aerosol contributes up to 60% of the non-

405   refractory PM$_1$ mass. Mobile AMS results from Gu et al. (2018) showed that cooking OA

406   contributes 5-20% of PM$_1$ mass over multiple areas in the city of Pittsburgh. Other

407   measurements in Pittsburgh also showed that cooking OA concentrations were clearly

408   elevated in the vicinity of restaurants when compared with residential areas (Robinson et

409   al., 2018). Though the cooking PM$_{2.5}$ mass predictions of our study cannot be directly

410   compared to these measurements, they all highlight the local importance of cooking as a

411   fine PM pollution source.

412   On average, the miscellaneous area sources sector contributes 0.26 µg m^{-3}

413   accounting for 4.3% of the PM$_{2.5}$. In downtown Pittsburgh, where the contribution is

414   highest, this source contributes 7% of the PM$_{2.5}$.

415   Unlike in the winter period, the plumes from major powerplants in the Ohio river

416   valley are clearly resolved in the summer. The power generation sector contributes a

417   maximum of 2.4 µg m^{-3} in the plume of the Bruce Mansfield power plant northwest of

418   Pittsburgh. On average, the 9.4% contribution from this sector to the PM$_{2.5}$ is much larger

419   than in the winter where it only contributed 2.3%. The plume from the Mitchell power

420   plant in the southwest corner of the modeling domain is clearly resolved and reaches all

421   the way to the city. This increases the contribution from power generation to the PM$_{2.5}$ in

422   the downtown core from 0.22 µg m^{-3} in the winter to 0.61 µg m^{-3} in the summer. The

423   maximum contribution of 8.98 µg m^{-3} from industrial sources is a cluster of industrial

424   facilities in the town of Beaver, northwest of Pittsburgh.

425   Long-range transport from sources outside the region contributes a maximum of

426   5.2 µg m^{-3} in the southeast corner of the domain decreasing in the direction of the Pittsburgh

427   northern suburbs where the contribution is minimal with 4.1 µg m^{-3}. On average, long-

428   range transport accounts for 72% of the PM$_{2.5}$ mass. In downtown Pittsburgh, long-range

429   transport contributes 4.24 µg m^{-3} accounting for 35% of the PM$_{2.5}$. The high-concentration

430   area visible on the western edge of the domain is due to a cluster of power generation and

431   industrial sources located in the Ohio River valley just outside of the inner modeling

432   domain.

433   On average, the contribution from all remaining sources is 3.6% and shows a

434   moderate variability of 0.1 µg m^{-3}. The contribution from these sources is maximal in

435   downtown Pittsburgh with 0.78 µg m^{-3} accounting for 6% of the PM$_{2.5}$.

436   For all local sources, the minimum contribution is close to zero (less than 0.1 µg

437   m^{-3}) and is located at the northwestern corner of the domain, near the Ohio – Pennsylvania

438   border.

439   Relative contributions of all local sources to domain average predicted total PM$_{2.5}$

440   (including long-range transport PM$_{2.5}$ mass) are shown in Figure 9. The largest differences

441   between February and July are the contributions from biomass burning and power

442   generation. In the winter, biomass burning is the most important local source of PM$_{2.5}$,

443   contributing over 8%. In the summer, this source contributes much less than 1% to total

444   PM$_{2.5}$. This discrepancy can easily be explained by the lack of residential wood combustion

445   in the warmer months of the year. Power generation is a significantly more important

446   source in July than in February. This is likely a result of a lower mixing height in the winter

447   combined with emissions plumes from power plants in the Ohio river vally originating

448   from very tall stacks.

449   The relative contributions of local sources to average predicted total PM$_{2.5}$ in the

450   maximum concentration cell in Beaver County and in downtown Pittsburgh are shown in

451   Figures 10 and 11, respectively. The dominant local source in the Beaver County location

452   is industrial emissions, due to the proximity of various industrial installations in this area.

453   Industrial sources here account for around 49% of total PM$_{2.5}$ in February and 58% of total

454   PM$_{2.5}$ in July. A lot of the difference in industrial PM$_{2.5}$ at the Beaver County location

455   between months is made up by biomass burning in February, which accounts for 7% more

456   of the total compared to July. In the downtown area of Pittsburgh, the majority of PM$_{2.5}$

457   from local sources can be attributed to either traffic (22-27% of total PM$_{2.5}$) or cooking

458   (16-18% of total PM$_{2.5}$) in both simulation periods (Figure 11).

459

6. Exposure to PM$_{2.5}$

The population data in the inner domain from the 2010 U.S. census was used to estimate the exposure of the population in the Pittsburgh area to model predictions of PM$_{2.5}$ during winter of 2017 at the different grid resolutions. We ranked the average PM$_{2.5}$ concentrations from all the cells in the modeling domain and created bins of 0.2 µg m^{-3}. A sum of the population from all the grid cells that fall within each concentration bin was calculated and divided by the total population of the inner grid to construct population exposure histograms. The population data used here is resolved at the census group level, which is much smaller than the simulation grid cell size of 1 x 1 km.

6.1 Winter PM$_{2.5}$ Exposure

Figure 12 shows the population exposure histograms for the Pittsburgh area (inner domain) for each model resolution. At the coarse resolution, there are only four PM$_{2.5}$ values and 46% of the population is exposed to a concentration of 10.4 µg m^{-3} with decreasing exposure with PM$_{2.5}$ concentration. At a 12 km resolution, the low concentration side of the distribution is better resolved but gaps can still be observed at higher levels. At this intermediate resolution, the largest fraction of the population (15%) is exposed to PM$_{2.5}$ concentrations of 11.8 µg m^{-3}.

When the resolution is increased to 4 km the biggest improvements on the model ability to resolve the exposure distribution happen at concentrations higher than 9.4 µg m^{-3}. At the fine resolution, no gaps appear in the distribution. A maximum of 12% of the population is exposed to PM$_{2.5}$ concentrations of 12 µg m^{-3} while at the highest concentration of 12.8 µg m^{-3} 3% are exposed. At the 1 km resolution, the distribution is much smoother due to the ability of this finest grid to capture local gradients. The largest fraction of the population (6%) is exposed to PM$_{2.5}$ concentrations of 9.2 µg m^{-3}. At the highest concentration of 14.4 µg m^{-3} the exposed population is less than 0.1% as this maximum point is located near industrial installations 37 km northwest of Pittsburgh where the population density is very low.

The differences between the predicted exposure distributions at 4 km and 1 km resolutions highlight the need for high resolution modeling studies in order to identify key areas from the environmental justice perspective. The upper tail of the exposure

491 distribution (13-14 µg m^{-3}) is only detectable at the 1 km resolution. These higher
492 exposures could be addressed by appropriate targeted regulations, because they are the
493 direct result of proximity to either major industrial and electrical generation sources or
494 dense traffic and cooking emissions.

495   At resolutions of 36 km, 12 km, 4 km, and 1 km the predicted average population
496 weighted total PM$_{2.5}$ concentration during February 2017 is 9.74 µg m^{-3}, 9.77 µg m^{-3}, 10.28
497 µg m^{-3}, and 10.00 µg m^{-3}, respectively. This represents an increase of only 2.6% when
498 moving from lowest to highest resolution. Relative contributions of local sources to
499 average population weighted PM$_{2.5}$ concentration is shown in Figure 14. Compared to the
500 domain average PM$_{2.5}$ concentrations (Figure 9), many local source contributions are
501 enhanced in terms of average population exposure. In February, weighting PM$_{2.5}$
502 concentrations by population increases the contribution from biomass burning from 8.3%
503 to 11.7%. Other notable increases include onroad traffic (2.5% to 6.5%), and miscellaneous
504 area sources (5.9% to 9.2%). Other local source contributions to population weighted PM$_{2.5}$
505 were similar to the corresponding non-weighted concentrations.

506   The source-resolved population exposure distributions during this winter period are
507 shown in Figures S6 and S7.

508

509 **6.2   Summer PM$_{2.5}$ Exposure**

510   Figure 13 shows the population exposure for each simulation grid during the
511 summer period. At the coarse resolution, 88% of the population is exposed to a
512 concentration of 7 to 7.2 µg m^{-3}. At 12 x 12 km resolution, the exposure distribution is
513 better resolved but a gap is still present at 7.2 µg m^{-3} and exposure to PM$_{2.5}$ concentrations
514 above 7.6 µg m^{-3} is not resolved at all. At this intermediate resolution, the largest fraction
515 of the population (19%) is exposed to PM$_{2.5}$ concentrations of 7.4 µg m^{-3}. Increasing the
516 resolution to 4 x 4 km both shifts the distribution to slightly lower concentrations and
517 resolves exposure to higher PM$_{2.5}$ concentrations than with the 12 x 12 km grid. At this
518 resolution, 14% of the population is exposed to 6.4 µg m^{-3} and smaller portions of the
519 population are exposed to concentrations higher than 8.0 µg m^{-3}. Moving to the highest
520 resolution grid further resolves the exposure distribution. Most notably, 1 x 1 km resolution
521 reveals a bimodal distribution of population exposure, with one peak centered around 6.0

522   $\mu g\ m^{-3}$ and another centered around 7.4 $\mu g\ m^{-3}$. This likely corresponds to one subset of

523   the population in the urban areas of Pittsburgh who are exposed to higher $PM_{2.5}$

524   concentrations and another subset representing the surrounding suburban areas.

525   In the summer period, an even larger range of high-concentration exposure is

526   revealed moving from 4 km to 1 km resolution. At this high resolution, the population

527   exposure to concentrations ranging from 8.5 $\mu g\ m^{-3}$ to 12 $\mu g\ m^{-3}$ becomes clear Most people

528   exposed to these higher fine PM levels according to PMCAMx live in the vicinity of the

529   industrial complexes and power stations around the city of Beaver. The higher

530   concentration range of the upper tail of the exposure during July compared to February is

531   due to a large extent to the effective mixing of the emissions from the tall stacks down to

532   the ground level.

533   At resolutions of 36 km, 12 km, 4 km, and 1 km the predicted average population

534   weighted total $PM_{2.5}$ concentration during February 2017 is 7.06 $\mu g\ m^{-3}$, 6.78 $\mu g\ m^{-3}$, 7.0

535   $\mu g\ m^{-3}$, and 6.99 $\mu g\ m^{-3}$, respectively. This represents just a 1% decrease between the

536   lowest and highest resolutions. Similar to the effect seen in February, weighting $PM_{2.5}$

537   concentrations by population increases the contribution from onroad traffic from 3.3% to

538   8.9% in July. Contributions from miscellaneous area sources also increased (4.3% to 7.1%)

539   when weighting by population. The population weighted contribution from power

540   generation sources in July decreased from the non-weighted value from 9.4% to 8.3%. All

541   other local source contributions to population weighted $PM_{2.5}$ in July were similar to the

542   non-weighted values.

543   The source-resolved population exposure distributions during this summer period are

544   shown in Figures S8 and S9.

545

546   **7. Conclusions**

547   We applied the PMCAMx chemical transport model over the city of Pittsburgh for

548   the simulation periods of February and July 2017 using a series of telescoping grids at 36

549   x 36 km, 12 x 12 km, 4 x 4 km and 1 x 1 km. Emissions were calculated using 2017

550   projections from the 2011 NEI. Emissions were distributed geographically using the spatial

551   surrogates provided with the NEI11 for all grids. For commercial cooking, a new 1 x 1 km

552   spatial surrogate was developed using restaurant count data from the Google Places API.

553 Traffic model data was used to develop a 1 x 1 km spatial surrogate for on-road traffic
554 emissions.

555   At the coarse resolution, county-level differences can be observed. Increasing the
556 resolution to 12 x 12 km resolves the urban-rural gradient and further increasing to 4 x 4
557 resolves large stationary sources such as power plants. Only at the finest resolution intra-
558 urban variations and individual roadways are resolved. Low variability, regional pollutants
559 such as nitrate show limited improvement after increasing the resolution to 12 x 12 km
560 while predominantly local pollutants such as elemental carbon and winter organic aerosol
561 have gradients that can only be resolved at the finest resolution.

562   Biomass burning shows the largest variability during the winter period with many
563 local maxima and significant emissions within the city and in the suburbs. During the
564 summer contributions from this source are negligible. In contrast with the winter period,
565 during the summer the plumes from large power plants in the Ohio river valley can be
566 resolved. These plumes are rich in sulfates and start being resolved at 4 x 4 km with
567 significant detail added at 1 x 1 km. During both periods the largest contributing source to
568 the average $PM_{2.5}$ is particles from outside the modeling domain.

569   The ability of the model to resolve the exposure distribution increases at different
570 rates according to the concentration. A significant improvement in resolving exposure to
571 concentrations below 9.4 µg m^{-3} in the winter and below 7.0 µg m^{-3} in the summer is
572 achieved by increasing the resolution to 12 x 12 km. Only at the finest resolution is the
573 exposure to concentrations above 9.6 µg m^{-3} in the winter and above 8.6 µg m^{-3} in the
574 summer fully resolved as well as the impact of high concentration spots.

575   The average exposure in terms of average contribution to population weighted
576 $PM_{2.5}$ concentrations of some local sources is enhanced compared to the non-weighted
577 average $PM_{2.5}$ concentrations. In February, weighting by population enhanced the
578 contributions from biomass burning, onroad traffic, and miscellaneous area sources by 3-
579 4%. In July, the contributions from onroad traffic and miscellaneous area sources also
580 increased by 3-5% from this procedure.

581   It was determined that increasing simulation grid resolution from 36 x 36 km to 1
582 x 1 km had minimal effect on the predicted domain average population weighted $PM_{2.5}$
583 concentration. Moving from the lowest to highest grid resolution increased the predicted

584 average population weighted $PM_{2.5}$ by less than 3%. In July, the average decreased by 1%.
585 This negligible change in the predicted average exposure to $PM_{2.5}$ suggests that extremely
586 high resolution predictions of urban $PM_{2.5}$ pollution may not be necessary for accurate
587 epidemiological analysis in the absence of high-resolution health data. However it is also
588 clear that the average population-weighted concentration approach misses the potentially
589 important impacts of large sources on small communities. The increased neighborhood
590 scale resolution is vital for identifying communities that are disproportionately exposed to
591 large sources of $PM_{2.5}$ pollution, which in our study represent the upper tail of the exposure
592 distributions in both simulation periods.

593

8. Code and data availability

595 The code and simulation results are available upon request
596 (spyros@chemeng.upatras.gr).

597

9. Supplement

599

10. Author contributions

601 P.G.R. and B.T.D. performed the PMCAMx simulations, analyzed the results and
602 wrote the manuscript. P.G.R. prepared the anthropogenic emissions and other inputs for
603 the simulations. I.K. set-up the WRF simulations and assisted in the preparation of the
604 meteorological inputs. S.N.P. and P.J.A. designed and coordinated the study and helped
605 in the writing of the paper. All authors reviewed and commented on the manuscript.

606

11. Competing interests

608 The authors declare that they have no conflict of interest.

609

610

12. Financial Support

612 This work was supported by the Center for Air, Climate, and Energy Solutions
613 (CACES) which was supported under Assistance Agreement No. R835873 awarded by the

614   U.S. Environmental Protection Agency and the Horizon-2020 Project REMEDIA of the

615   European Union under grant agreement No 874753.

616

617

13. References

Anand, S.: The concern for equity in health. Journal of Epidemiology & Community Health 56, 485–487, 2002.

Arunachalam, S., Holland, A., Do, B., Abraczinskas, M.: A quantitative assessment of the influence of grid resolution on predictions of future-year air quality in North Carolina, USA. Atmospheric Environment 40, 5010–5026, 2006.

Carter, W. P. L.: Documentation of the SAPRC-99 chemical mechanism for VOC reactivity assessment, 1999.

Day, M., Pouliot, G., Hunt, S., Baker, K.R., Beardsley, M., Frost, G., Mobley, D., Simon, H., Henderson, B., Yelverton, T., Rao, V.: Reflecting on progress since the 2005 NARSTO emissions inventory report. Journal of the Air & Waste Management Association 69, 1025–1050, 2019.

Dockery, D. W., Pope, C. A.: Acute respiratory effects of particulate air pollution. Annual Review of Public Health 15, 107–132, 1994.

Donahue N. M., Robinson, A. L., Stanier, C. O., Pandis, S. N.: Coupled partitioning, dilution, and chemical aging of semivolatile organics. Environmental Science & Technology, 40, 2635-2643, 2006.

Elessa Etuman, A., Coll, I.: OLYMPUS v1.0: Development of an integrated air pollutant and GHG urban emissions model-methodology and calibration over greater Paris. Geoscientific Model Development 11, 5085–5111, 2018.

ENVIRON: CAMx (Comprehensive Air Quality Model with Extensions) User's Guide Version 4.20, 2005.

Eyth, A., Vukovich, J.: Technical Support Document (TSD): Preparation of Emissions Inventories for the Version 6.2, 2011 Emissions Modeling Platform, 2016.

Fahey, K. M.; Pandis, S. N.: Optimizing model performance: variable size resolution in cloud chemistry modeling. Atmospheric Environment, 35, 4471-4478, 2001.

Fountoukis, C., Koraj, D., Denier van der Gon, H. A. C., Charalampidis, P. E., Pilinis, C., Pandis, S. N.: Impact of grid resolution on the predicted fine PM by a regional 3-D chemical transport model. Atmospheric Environment 68, 24–32, 2013.

Fountoukis, C., Racherla, P. N., Denier van der Gon, H. A. C., Polymeneas, P., Charalampidis, P. E., Pilinis, C., Wiedensohler, A., Dall'Osto, M., O'Dowd, C.,

649   Pandis, S. N.: Evaluation of a three-dimensional chemical transport model
650   (PMCAMx) in the European domain during the EUCAARI May 2008 campaign.
651   Atmospheric Chemistry and Physics 11, 10331–10347, 2011.

652   Gilliam, R. C., Pleim, J. E.: Performance assessment of new land surface and planetary
653   boundary layer physics in the WRF-ARW. Journal of Applied Meteorology and
654   Climatology 49, 760-774, 2010.

655   Gu, P., Li, H. Z., Ye, Q., Robinson, E. S., Apte, J. S., Robinson, A. L., Presto, A. A.:
656   Intracity variability of particulate matter exposure is driven by carbonaceous sources
657   and correlated with land-use variables. Environmental Science and Technology 52,
658   11545–11554, 2018.

659   Hogrefe, C., Pouliot, G., Wong, D., Torian, A., Roselle, S., Pleim, J., Mathur, R.: Annual
660   application and evaluation of the online coupled WRF-CMAQ system over North
661   America under AQMEII phase 2. Atmospheric Environment 115, 683–694, 2015.

662   Karydis, V. A., Tsimpidi, A. P., Fountoukis, C., Nenes, A., Zavala, M., Lei, W., Molina,
663   L. T., Pandis, S. N.: Simulating the fine and coarse inorganic particulate matter
664   concentrations in a polluted megacity. Atmospheric Environment 44, 608-620, 2010.

665   Kumar, N., Russell, A. G.: Multiscale air quality modeling of the Northeastern United
666   States. Atmospheric Environment 30, 1099–1116, 1996.

667   Lane, T. E., Donahue, N. M., Pandis, S. N.: Effect of NO_x on secondary organic aerosol
668   concentrations. Environmental Science & Technology 42, 6022–6027, 2008.

669   Ma, W., Pi, X., Qian, S.: Estimating multi-class dynamic origin-destination demand
670   through a forward-backward algorithm on computational graphs. Transportation
671   Research Part C: Emerging Technologies, 119, 102747, doi:10.1016/j.trc.2020.
672   102747, 2020.

673   McDonald, B., McBride, Z.: High-resolution mapping of motor vehicle carbon dioxide
674   emissions. Journal of Geophysical Research, 119, 5283–5298, 2014.

675   Murphy, B. N., Pandis, S. N.: Simulating the formation of semivolatile primary and
676   secondary organic aerosol in a regional chemical transport model. Environmental
677   Science & Technology, 43, 4722-4728, 2009.

678   Nenes A., Pandis, S. N., Pilinis, C.: ISORROPIA: A new thermodynamic equilibrium
679   model for multiphase multicomponent inorganic aerosols. Aquatic Geochemistry, 4,

680   123-152, 1998.

681 Pan, S., Choi, Y., Roy, A., Jeon, W.: Allocating emissions to 4 km and 1 km horizontal

682   spatial resolutions and its impact on simulated NO_x and O_3 in Houston, TX.

683   Atmospheric Environment 164, 398–415, 2017.

684 Pandis, S. N., Wexler, A. S., Seinfeld, J. H.: Secondary organic aerosol formation and

685   transport - II. Predicting the ambient secondary organic aerosol size distribution.

686   Atmospheric Environment, 27, 2403–2416, 1993.

687 Robinson, E. S., Gu, P., Ye, Q., Li, H. Z., Shah, R. U., Apte, J. S., Robinson, A. L., Presto,

688   A. A.: Restaurant impacts on outdoor air quality: Elevated organic aerosol mass from

689   restaurant cooking with neighborhood-scale plume extents. Environmental Science

690   and Technology 52, 9285–9294, 2018.

691 Rogers, R. E., Deng, A., Stauffer, D. R., Gaudet, B. J., Jia, Y., Soong, S. T., Tanrikulu, S.:

692   Application of the weather research and forecasting model for air quality modeling in

693   the San Francisco bay area. Journal of Applied Meteorology and Climatology 52,

694   1953–1973, 2013.

695 Seinfeld, J. H., Pandis, S. N.: Atmospheric Chemistry and Physics: From Air Pollution to

696   Climate Change, 2nd. ed. John Wiley & Sons, Inc., Hoboken, 2006.

697 Stroud, C. A., Makar, P. A., Moran, M. D., Gong, W., Gong, S., Zhang, J., Hayden, K.,

698   Mihele, C., Brook, J. R., Abbatt, J. P. D., Slowik, J. G.: Impact of model grid spacing

699   on regional- and urban-scale air quality predictions of organic aerosol. Atmospheric

700   Chemistry and Physics 11, 3107–3118, 2011.

701 Tsimpidi, A. P., Karydis, V. A., Zavala, M., Lei, W., Molina, L., Ulbrich, I. M., Jimenez,

702   J. L., Pandis, S. N.: Evaluation of the volatility basis-set approach for the simulation

703   of organic aerosol formation in the Mexico City metropolitan area. Atmospheric

704   Chemistry and Physics, 10, 525-546, 2010.

705 United States Environmental Protection Agency: 2011 National Emissions Inventory,

706   version 2 Technical Support Document, 2015.

707 Ye, Q., Gu, P., Li, H. Z., Robinson, E. S., Lipsky, E., Kaltsounoudis, C., Lee, A. K. Y.,

708   Apte, J. S., Robinson, A. L., Sullivan, R. C., Presto, A. A., Donahue, N. M.: Spatial

709   variability of sources and mixing state of atmospheric particles in a metropolitan area.

710   Environmental Science & Technology, 52, 6807-6815, 2018.

711   Zakoura, M., Pandis, S. N.: Improving fine aerosol nitrate predictions using a Plume-in-
712   Grid modeling approach. Atmospheric Environment 116887, doi:10.1016/j.atmosenv.
713   2019.116887, 2019.

714   Zakoura, M., Pandis, S. N.:. Overprediction of aerosol nitrate by chemical transport
715   models: The role of grid resolution. Atmospheric Environment 187, 390–400, 2018.

716

717

718

719 **Table 1.** PM$_{2.5}$ emissions by source for the 1 x 1 km Pittsburgh domain (February 2017).

720

Source Type	Emissions (kg d^{-1} km^{-2})								
	PM$_{2.5}$	OA	EC	Chl.	Na	Amm.	Nitrate	Sulfate	Other
Agricultural dust	68.7	9.7	0.4	0.2	0.1	0.1	0.1	0.7	57.2
River barges	19.0	4.2	14.7	0.0	0.0	0.0	0.0	0.1	0.1
Cooking	242	223	8.3	2.2	0.8	0.0	1.1	0.6	6.0
Misc. area sources	683	445	56.7	30.5	3.0	5.6	1.7	42	97.8
Off-road	147	56.2	73.1	0.3	0.1	0.0	0.3	1.1	16.1
Oil-gas (Area)	35.3	1.7	0.0	0.0	0.0	0.0	0.1	8.3	23.2
On-road traffic	188	84.6	75.2	0.3	0.1	1.8	0.6	8.3	16.4
Rail	40.7	8.9	31.4	0.0	0.0	0.0	0.0	0.1	0.2
Biomass burning	1,869	1,696	105	5.6	1.8	2.8	3.6	7.7	46.3
Power generation	3,517	201	194	2.8	0.0	15.7	2.6	460	2,641
Industrial	1,106	192	134	79.4	65.3	10.1	21.1	173	428
Oil-gas (point)	2.8	1.0	1.1	0.0	0.0	0.0	0.1	0.2	0.5

721

722 **Table 2.** PM$_{2.5}$ emissions by source for the 1 x 1 km Pittsburgh domain (July 2017).

723

Source Type	Emissions (kg d^{-1} km^{-2})								
	PM$_{2.5}$	OA	EC	Chl.	Na	Amm.	Nitrate	Sulfate	Other
Agricultural dust	67.3	8.9	0.4	0.1	0.1	0.1	0.1	0.7	56.9
River barges	19.0	4.2	14.7	0.0	0.0	0.0	0.0	0.1	0.1
Cooking	242	223	8.3	2.2	0.8	0.0	1.1	0.6	6
Misc. area sources	593	392	49.1	28.5	2.5	5.3	1.1	33	81.6
Off-road	205	83.5	92.9	0.2	0.1	0.0	0.4	1.1	27.3
Oil-gas (Area)	35.9	1.9	0.0	0.0	0.0	0.0	0.1	8.9	25.0
On-road traffic	162	67.6	66	0.4	0.1	1.5	0.5	8.6	17.2
Rail	40.7	8.9	31.4	0.0	0.0	0.0	0.0	0.1	0.2
Biomass burning	24.3	22	1.4	0.0	0.0	0.0	0.0	0.1	0.6
Power generation	3,780	216	208	3.1	0.0	16.9	2.8	495	2,840
Industrial	1,050	188	133	67.3	56.2	9.9	21.0	165	412
Oil-gas (point)	2.8	1.0	1.1	0.0	0.0	0.0	0.1	0.2	0.5

724

725

726

727
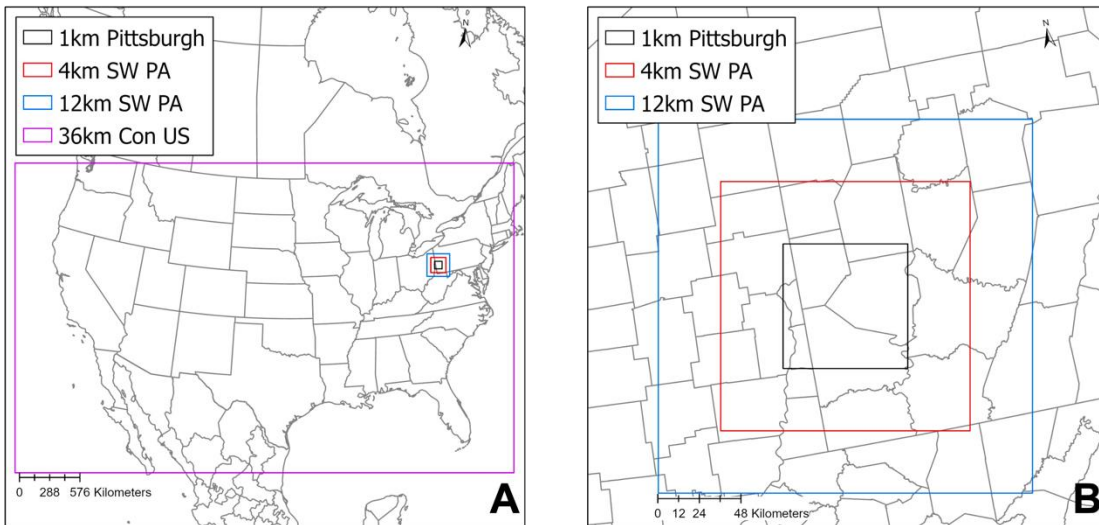
Figure 1. Modeling domain used for the PMCAMx simulations. (**A**) 36 x 36 km continental U.S. grid. (**B**) 12 x 12 and 4 x 4 km South Western Pennsylvania grids, and 1 x 1 km Pittsburgh nested grids.

731

732

733
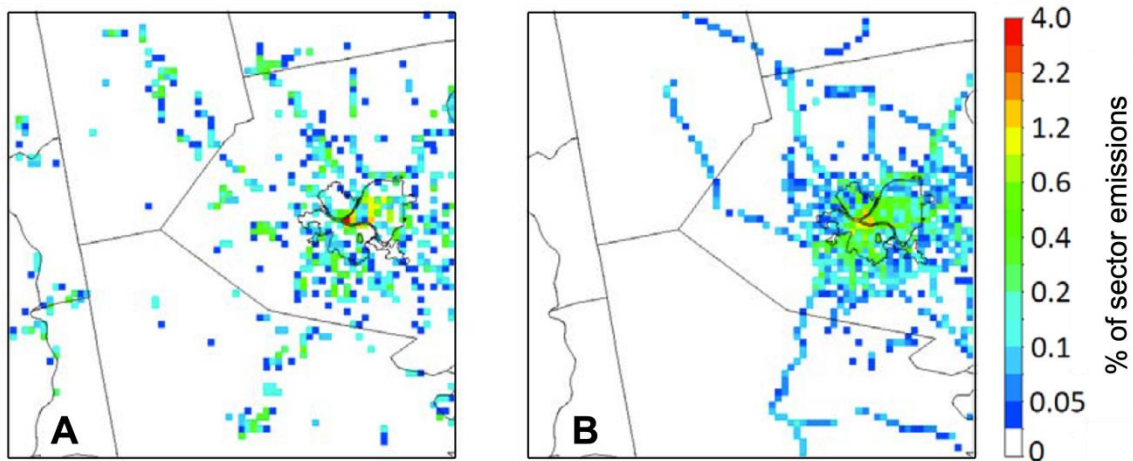
Figure 2. Percentage of sector PM$_{2.5}$ emissions in each 1x1 km computational cell for: (**A**) commercial cooking and (**B**) on road traffic in February 2017. The value of the colored points in each map add up to unity, corresponding to 100% of emissions for the respective sector.

738

739

740

741
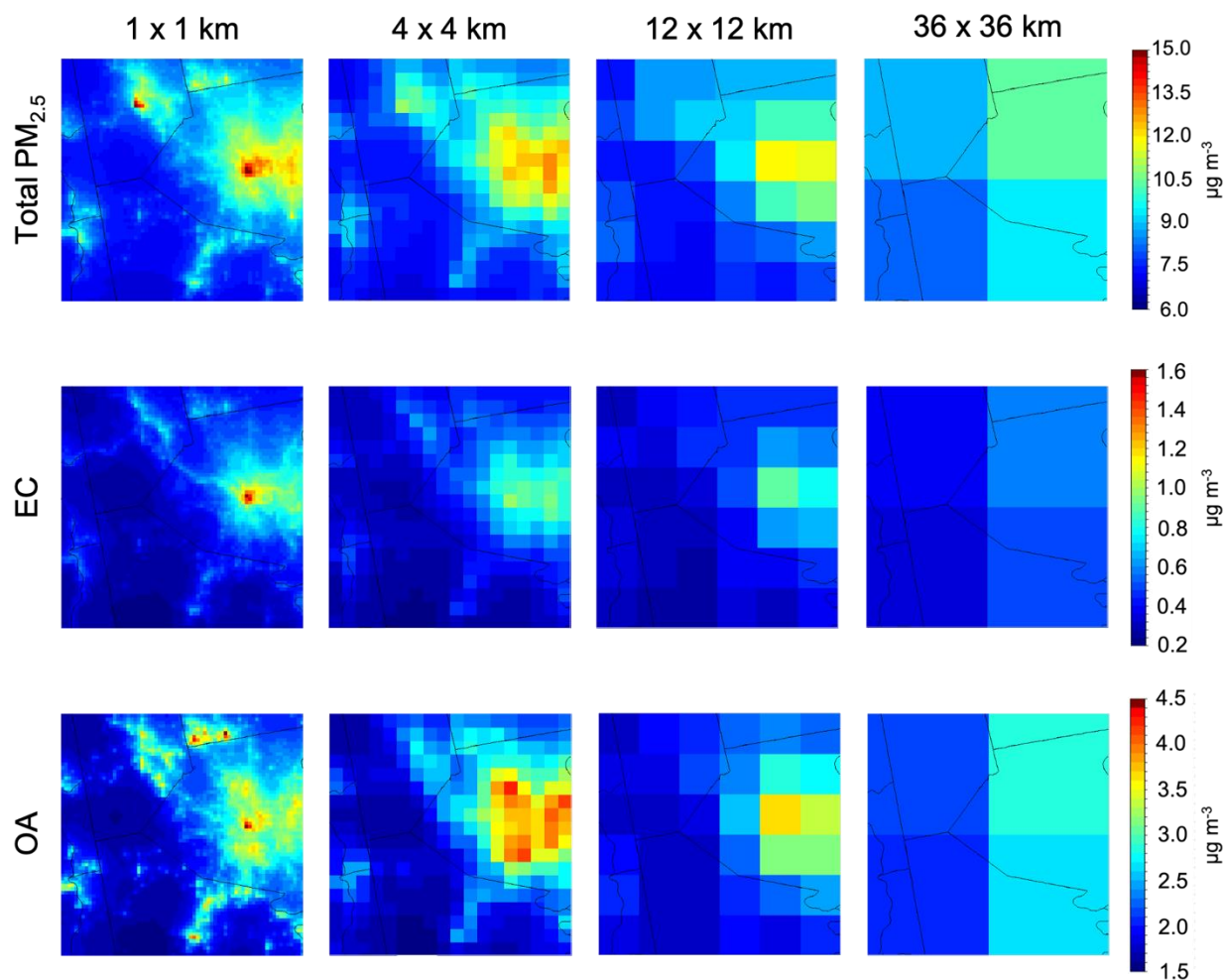
Figure 3. Average predicted ground-level concentration of total PM$_{2.5}$, EC, and OA at 36

x 36, 12 x 12, 4 x 4 and 1 x 1 km resolutions during February 2017. Different color scales

that do not start from zero are used for the various maps.

745

746

747

748
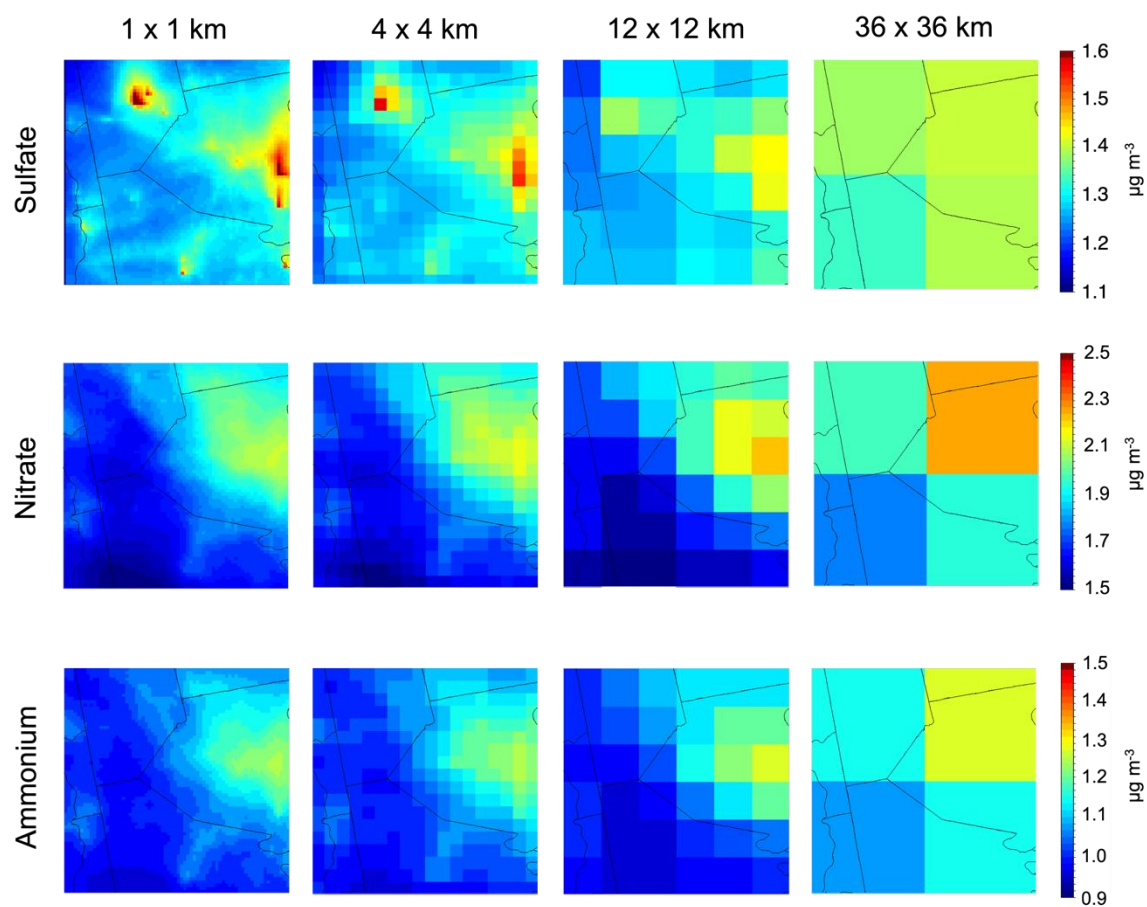
Figure 4. Average predicted ground-level concentration of PM$_{2.5}$ sulfate, nitrate and ammonium at a 36 x 36, 12 x 12, 4 x 4 and 1 x 1 km resolution during February 2017. Different color scales that do not start from zero are used for the various maps.

752

753

754

755

756
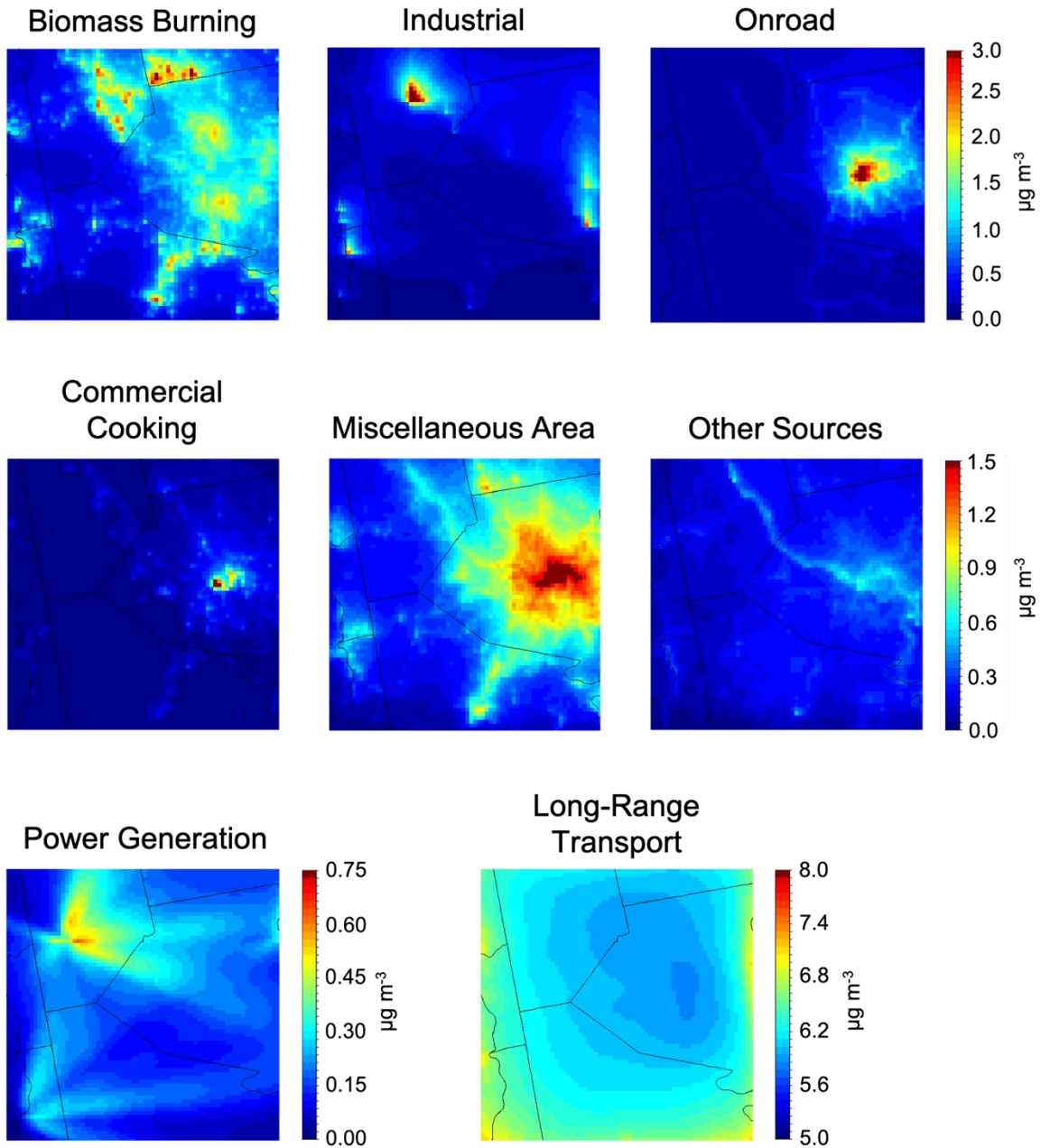
Figure 5. Contribution of each source to total PM$_{2.5}$ during February 2017. Different scales are used for the various maps.

759

760
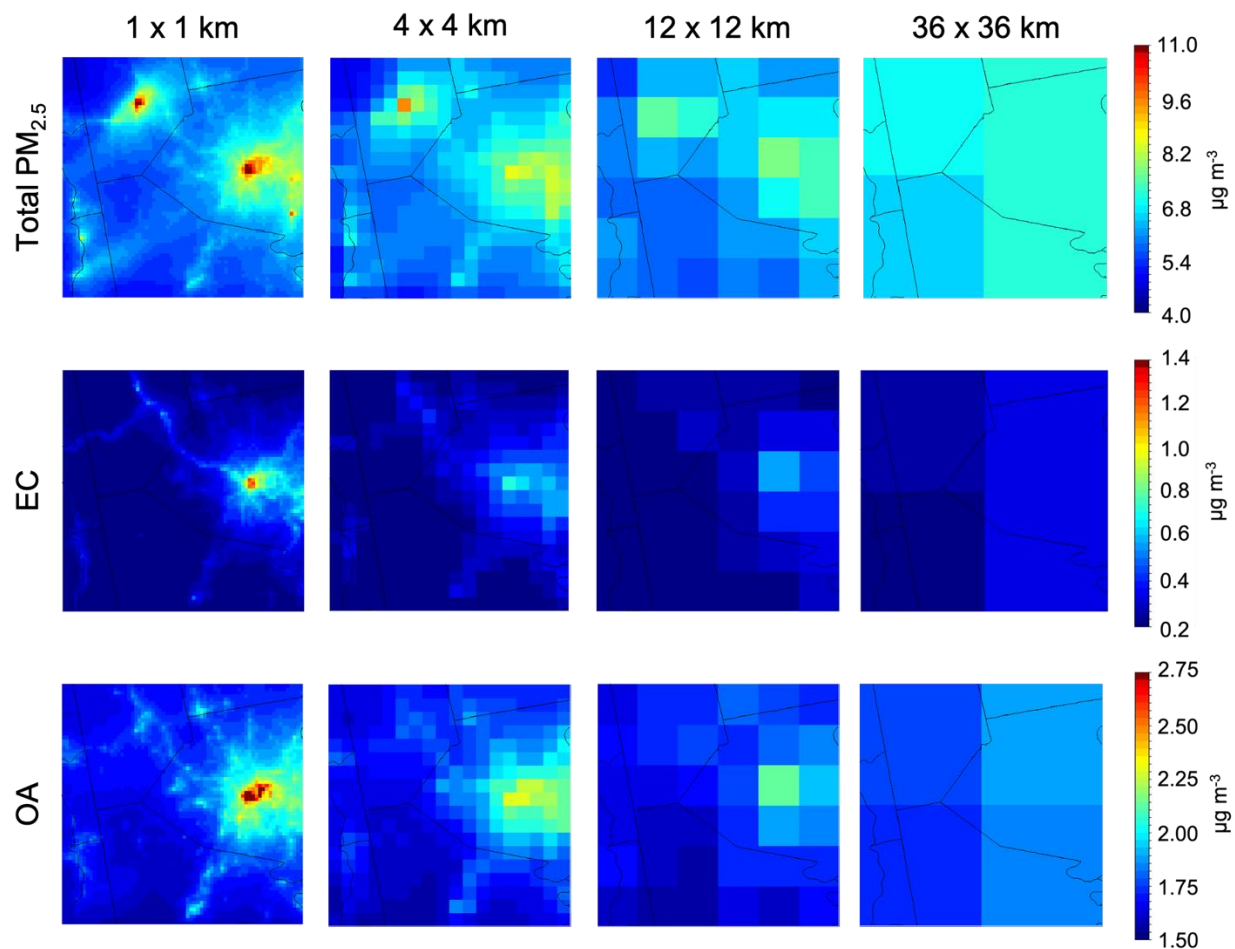
761

762 **Figure 6.** Average predicted concentration at the ground level of total $PM_{2.5}$, EC and OA

763 at a 36x36, 12x12, 4x4 and 1x1 km during July 2017. Different color scales that do not

764 start from zero are used for the various maps.

765

766

767
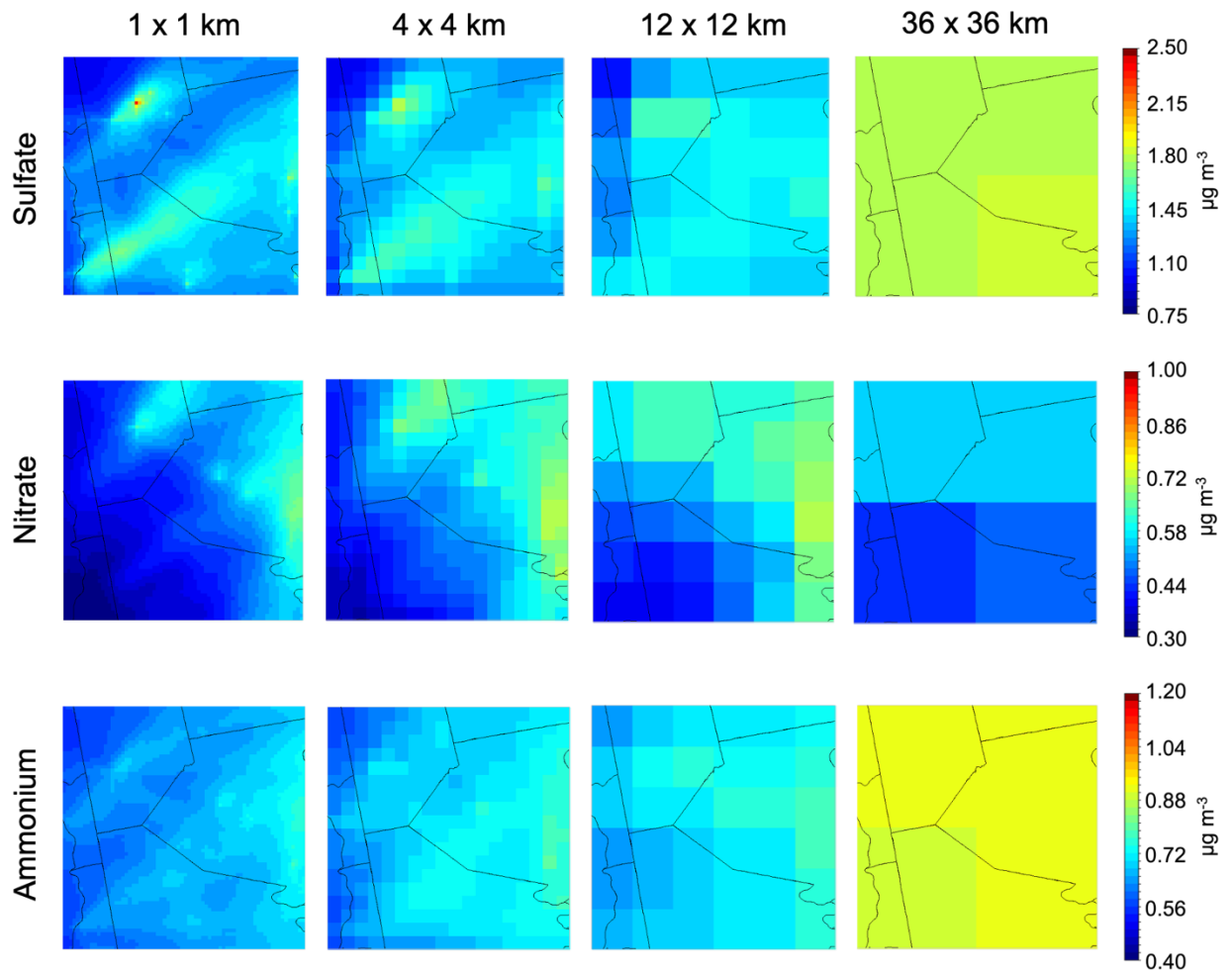
768

769 **Figure 7.** Average predicted concentration of PM$_{2.5}$ sulfate, nitrate, and ammonium at a

770 36x36, 12x 12, 4x4 and 1x1 km during July 2017. Different color scales that do not start

771 from zero are used for the various maps.

772

773
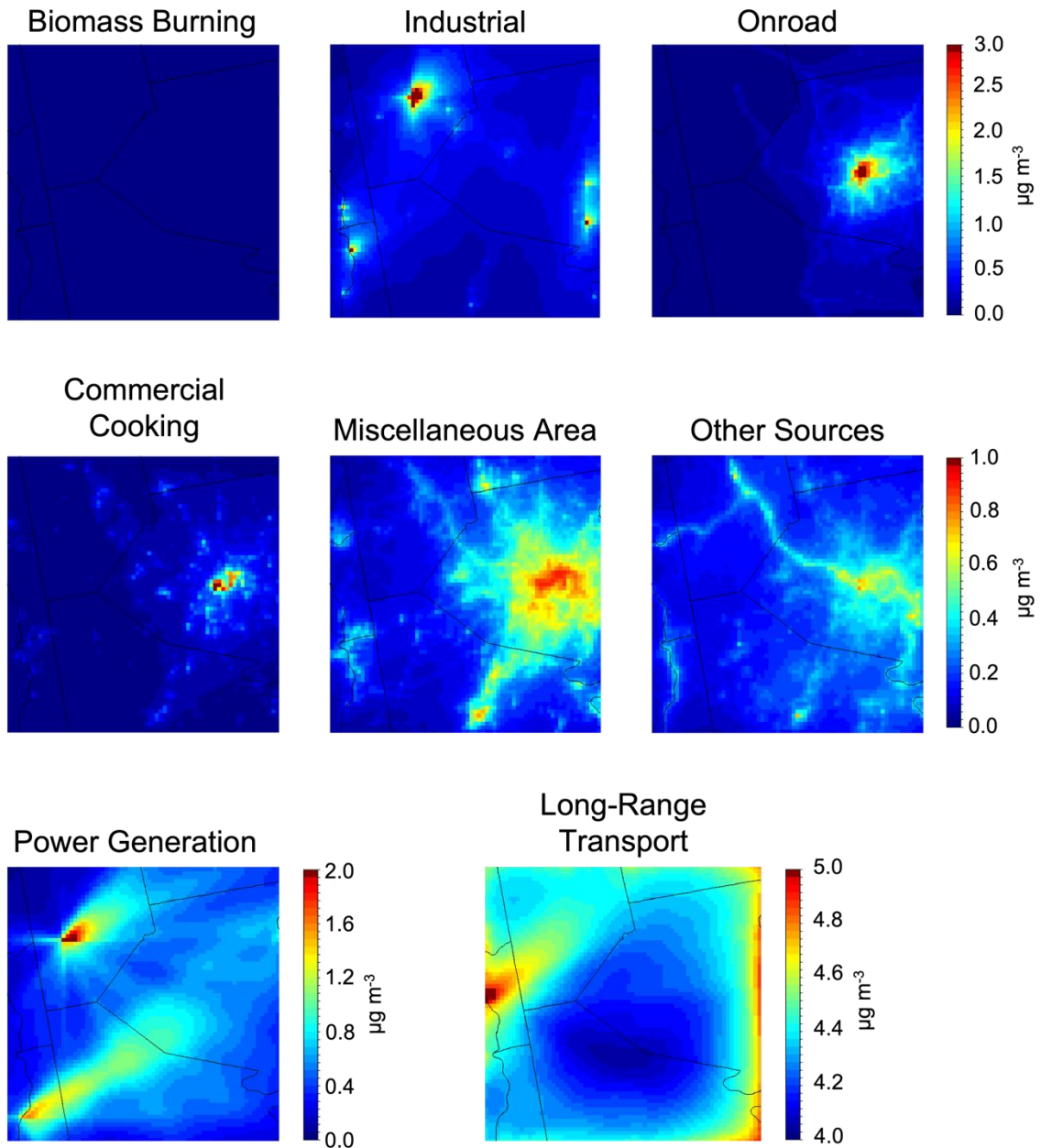
774

775

776 **Figure 8.** Contribution of each source to total PM$_{2.5}$ during July 2017. Different scales are

777 used for the various maps.

778

779

780
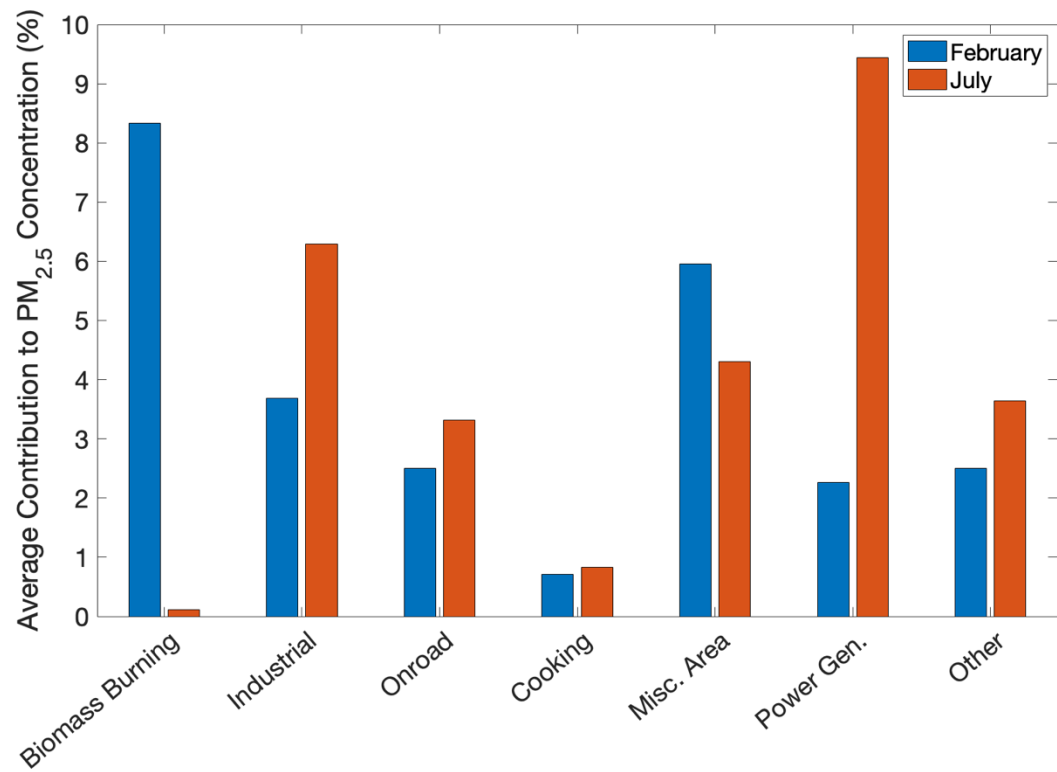
Figure 9. Relative contributions of local sources to average predicted total PM$_{2.5}$ concentrations in the inner 1x1 km resolution domain during February and July 2017.

783
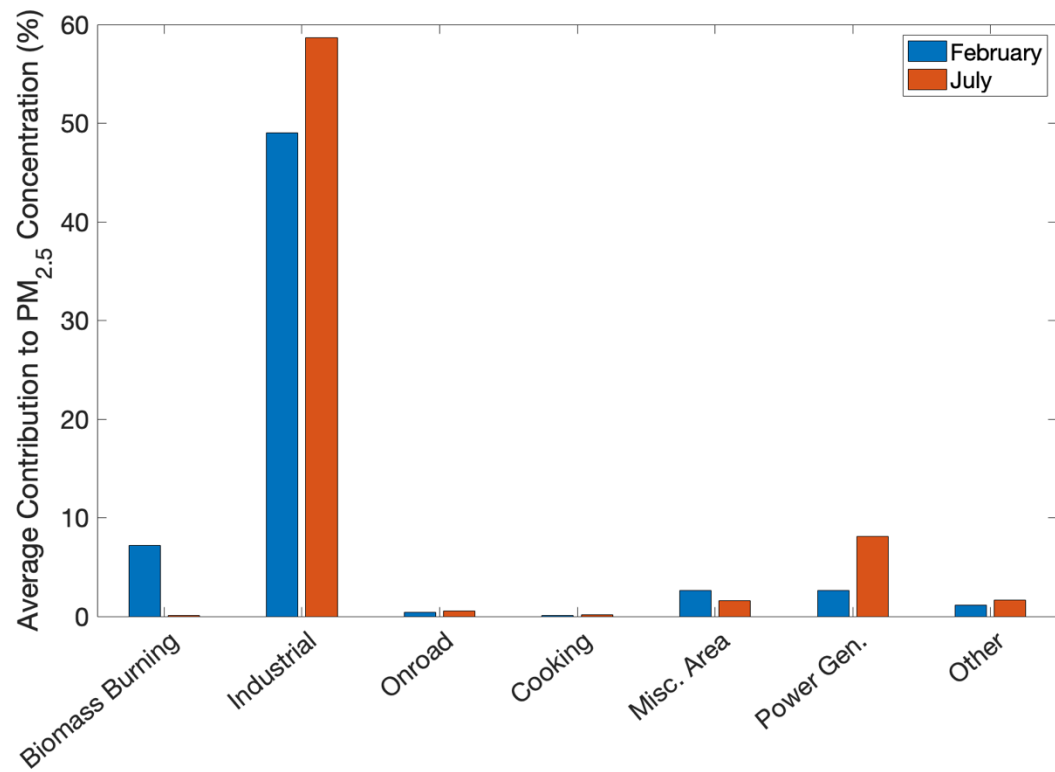
784

785   **Figure 10.** Relative contributions of local sources to average predicted PM$_{2.5}$

786   concentrations at the location of highest average concentration (Beaver County) during

787   February and July 2017.

788
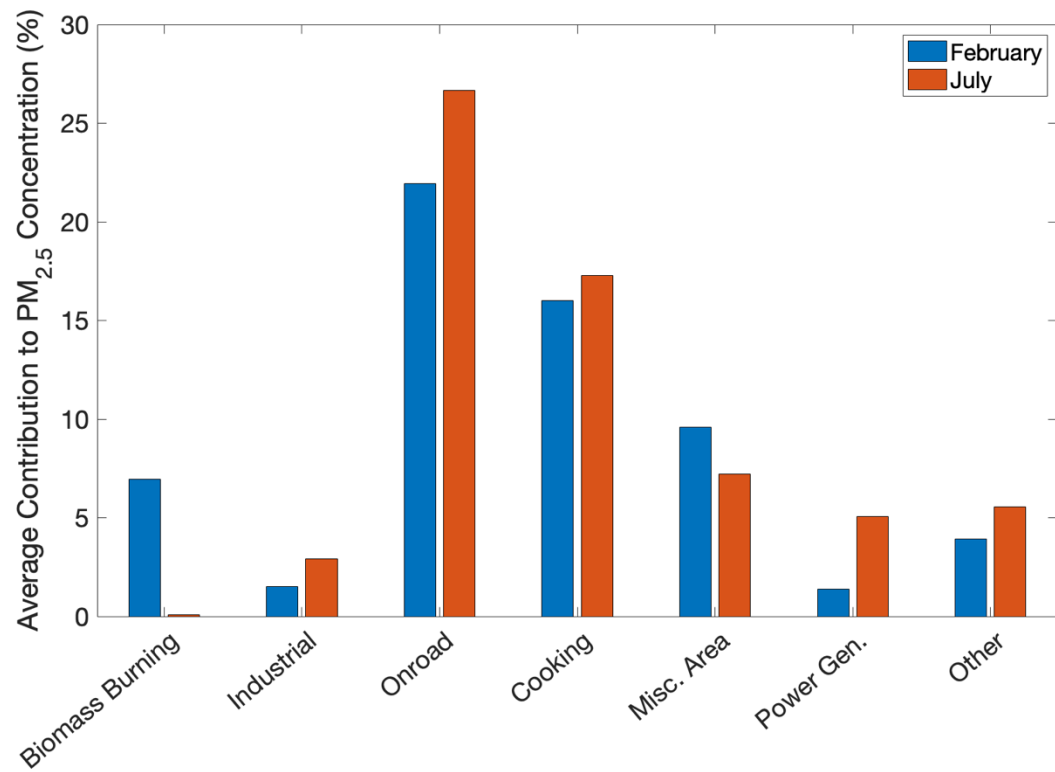
789

790 **Figure 11.** Relative contributions of local sources to average predicted total PM$_{2.5}$

791 concentrations in downtown Pittsburgh during February and July 2017.

792

793
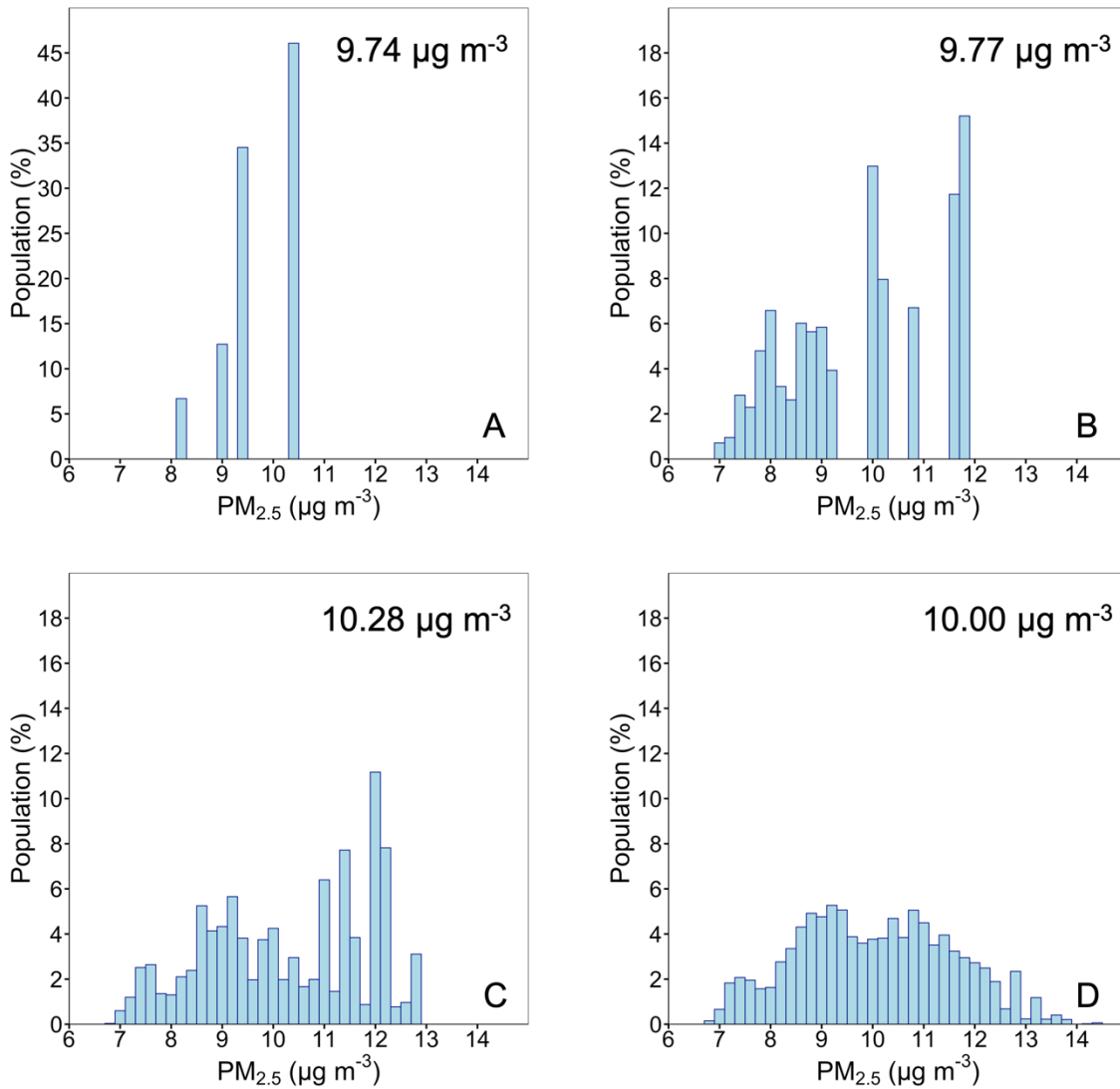
794

795

796 **Figure 12.** Population exposure histograms at (**A**) 36x36, (**B**) 12x 12, (**C**) 4x4 and (**D**) 1x1

797 km during February 2017. A different scale for population is used for the distribution at 36

798 x 36 km resolution. The average population weighted $PM_{2.5}$ concentration for each

799 resolution is shown in the upper right corner of each window.

800

801

802
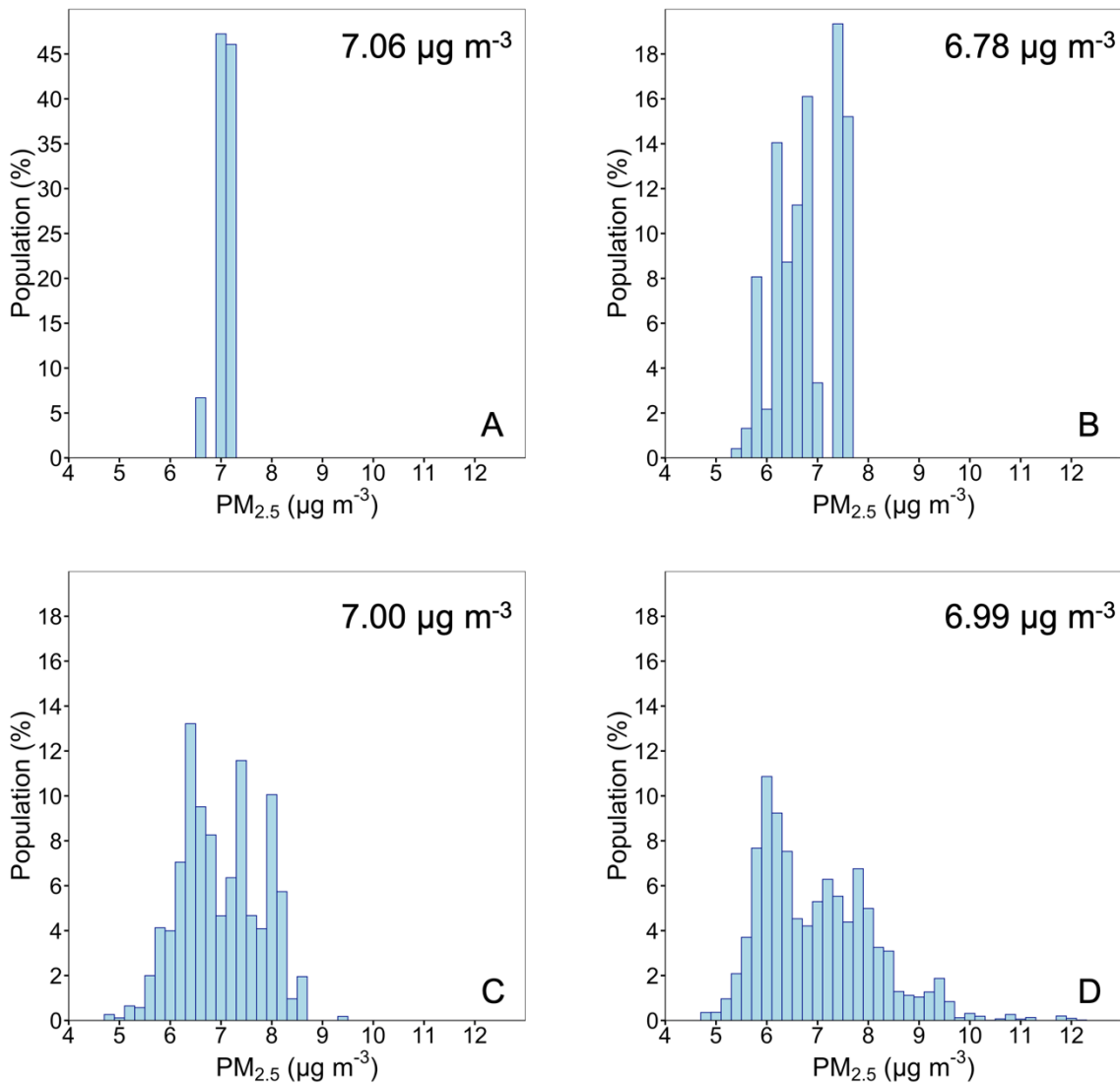
803 **Figure 13.** Population exposure histograms at (**A**) 36x36, (**B**) 12x 12, (**C**) 4x4 and (**D**) 1x1

804 km during July 2017. A different scale for population is used for the distribution at 36 x 36

805 km resolution. The average population weighted $PM_{2.5}$ concentration for each resolution is

806 shown in the upper right corner of each window.

807

809

810
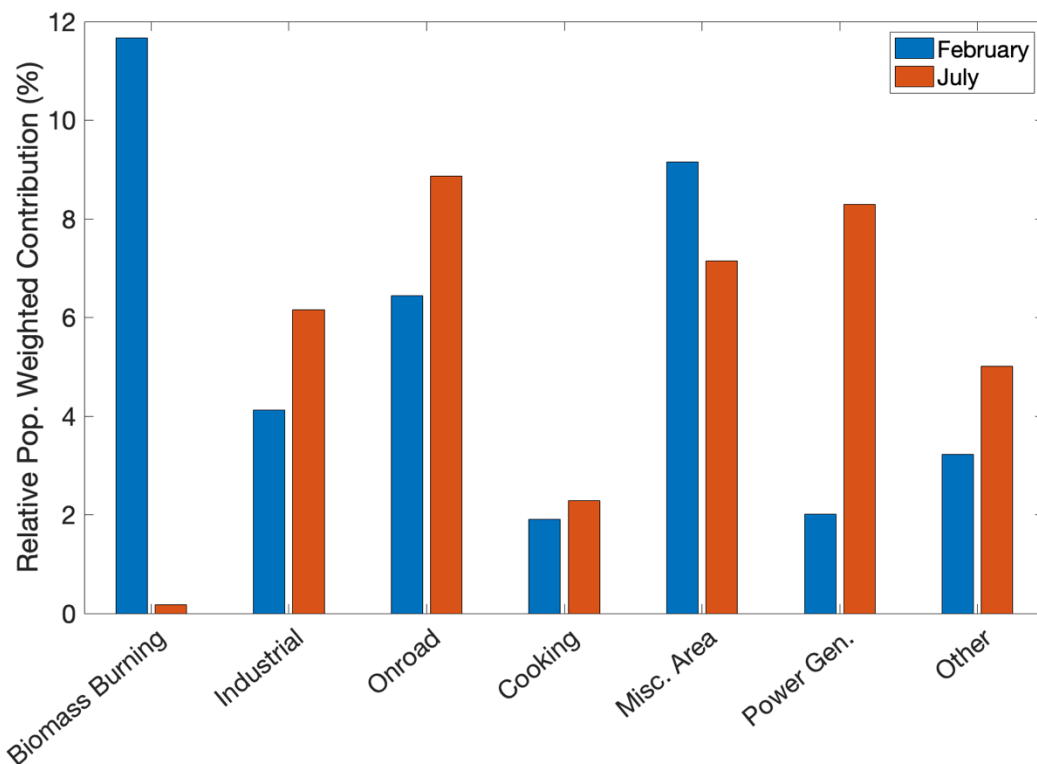
Figure 14. Relative contributions from local sources to population weighted total $PM_{2.5}$ concentration for February and July 2017.

813